

RESEARCH ARTICLE

Modulation of Exchange Bias in $\text{La}_{0.35}\text{Sr}_{0.65}\text{MnO}_3/\text{La}_{0.7}\text{Sr}_{0.3}\text{MnO}_3$ through Volatile Polarization of P(VDF-TrFE) Gate Dielectric

Xu Wen Zhao, Hon Fai Wong, Yu Kuai Liu, Sheung Mei Ng, Min Gan, Lok Wing Wong, Jiong Zhao, Zongrong Wang, Wang Fai Cheng, Chuanwei Huang, Linfeng Fei,*
Chee Leung Mak, and Chi Wah Leung*

Electric-field regulation of magnetic properties in perovskite manganites has attracted much attention for its potential in spintronics. For antiferromagnetic perovskite manganites, fewer studies are reported due to technological difficulties in probing their magnetic properties. Here, negative exchange bias (EB) is realized in epitaxial antiferromagnetic/ferromagnetic manganite bilayers with atomically flat interfaces. The low-voltage pulse modulation of EB is demonstrated using the field-effect device geometry with the ferroelectric copolymer, polyvinylidene fluoride with trifluoroethylene as a dielectric gating layer, antiferromagnetic $\text{La}_{0.35}\text{Sr}_{0.65}\text{MnO}_3$ (AF-LSMO) as pinning layer, and ferromagnetic $\text{La}_{0.7}\text{Sr}_{0.3}\text{MnO}_3$ (FM-LSMO) as conduction channel. Instead of using non-volatile polarizations to control the EB, volatile polarizations in ferroelectric field effect transistors are suggested to be capable of modulating the EB. With high-resolution electron microscopy and spectroscopy, the non-volatile regulation of EB is attributed to the creation/annihilation of oxygen vacancies in the AF-LSMO layer via low-voltage pulses. This study reveals the effect of volatile electric polarizations in ferroelectric field effect devices and highlights the potential for low-voltage pulse control of the physical properties in antiferromagnetic perovskite oxide insulators.

explain the essential EB features qualitatively. Recent studies on epitaxial systems suggested that bulk AF magnetic structures play a crucial role in determining EB.^[5–12] For example, the domain state model^[13] theorizes that bulk AF domain structures are stabilized by nonmagnetic defects when it is field cooled below the Néel temperature (T_N), and these domains carry pinned uncompensated magnetic spins and result in EB of the FM layer.

The possibility of manipulating EB in heterostructures by external means (such as electric field) can be of remarkable importance in terms of device applications, and will also shed light on the further understanding of EB. Breakthroughs along this direction have been made based on magnetoelectric coupling effect in AF insulators,^[14–16] ferroelectric polarization in ferroelectric/FM heterostructures,^[17,18]

and electrochemical reactions in magnetoionic devices.^[19–23]


Ferroelectric copolymer of polyvinylidene fluoride with trifluoroethylene (P(VDF-TrFE)) has been widely used in organic field effect transistors (FET).^[24] Meanwhile, reports on utilizing

1. Introduction

Early models of exchange bias (EB)^[1–4] considered the ferromagnetic (FM)/antiferromagnetic (AF) interfaces, and managed to

X. W. Zhao, H. F. Wong, S. M. Ng, L. W. Wong, J. Zhao, W. F. Cheng,
C. L. Mak, C. W. Leung
Department of Applied Physics
The Hong Kong Polytechnic University
Hung Hom, Hong Kong China
E-mail: dennis.leung@polyu.edu.hk

Y. K. Liu
College of Electronic Information and Mechatronic Engineering
Zhaoqing University
Zhaoqing, Guangdong 526061, China

 The ORCID identification number(s) for the author(s) of this article can be found under <https://doi.org/10.1002/admi.202300296>

© 2023 The Authors. Advanced Materials Interfaces published by Wiley-VCH GmbH. This is an open access article under the terms of the Creative Commons Attribution License, which permits use, distribution and reproduction in any medium, provided the original work is properly cited.

DOI: 10.1002/admi.202300296

M. Gan, L. Fei
School of Physics and Material Science
Nanchang University
Nanchang, Jiangxi 330031, China
E-mail: flf@ncu.edu.cn

Z. Wang
School of Aeronautics and Astronautics
Zhejiang University
Hangzhou 310027, China

C. Huang
Shenzhen Key Laboratory of Special Functional Materials
College of Materials Science and Engineering
Shenzhen University
Guangdong 518060, China

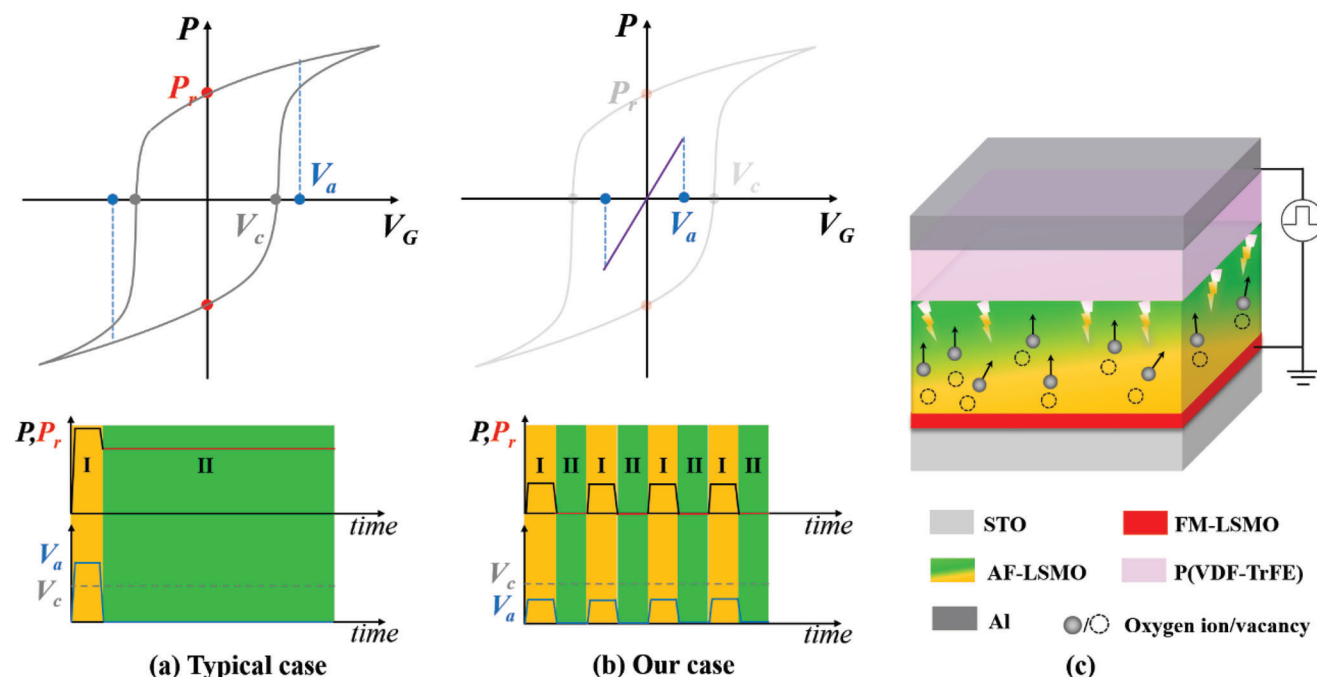


Figure 1. Low-voltage pulse regulation of EB in AF-LSMO/FM-LSMO. a) In typical ferroelectric field effect devices, the application of V_a across the ferroelectric layer leads to certain polarization (highlighted as “I” in lower panel). Once V_a is removed, the remnant polarization (P_r) retains, electrostatically dopes the channel layer and modulates its physical properties. b) In this study, V_a is sufficiently small that the remnant polarization is effectively zero. Exploration of the impact from those charges generated and then subsequently removed can therefore be realized. c) Illustration of FET device structure used in this work.

P(VDF-TrFE) as the gating material to modulate the magnetism in inorganic materials are rather limited. Due to the large mismatch of stiffness coefficients between P(VDF-TrFE) and inorganic materials, such studies are confined in using the remnant polarization (P_r) (Figure 1a) to control the magnetism, as realized in ultrathin Co^[25] and (Ga,Mn)As^[26] structures. In these cases, P_r (related to the ferroelectric domain switching and non-volatility after removing the applied voltage (V_a), region II in Figure 1a lower panel) is usually considered responsible for non-volatile modulation of physical properties. However, additional polarizations in surplus of P_r , due to the high dielectric constants of ferroelectric gates, are generated during the gating process, which is lost after electric field removal (region I in Figure 1a lower panel). The role of these volatile polarizations is rarely explored in ferroelectric field effect devices.^[27–29] To determine the actual influence of these additional charges, a new strategy is designed (Figure 1b): by setting V_a below the coercive voltage (V_c), a zero P_r is guaranteed after removing V_a (Figure S1, Supporting Information). The method was used recently to tune the properties in La_{0.7}Sr_{0.3}MnO₃ (FM-LSMO) and AF-La_{0.35}Sr_{0.65}MnO₃ (AF-LSMO) single layers.^[30–32]

Here we use the strategy (Figure 1b) to regulate EB effect in an AF-LSMO/FM-LSMO bilayer and probe the effect by magnetoresistance (MR) measurement. FM-LSMO is employed as the conductive channel because of its relative high Currie temperature ($T_C \approx 370$ K).^[33] The high structural compatibility between FM-LSMO and AF-LSMO allows coherent growth with atomic flat interface. It is anticipated that oxygen vacancies are created in the AF-LSMO layer (Figure 1c). Therefore, (depth-dependent)

changes of lattice structure and Mn oxidation state in the bilayer were probed by scanning transmission electron microscopy (STEM) and electron energy loss spectroscopy (EELS). Compared with negative pulses, positive pulses result in extensive oxygen deficiencies in the AF-LSMO layer, suggesting suppressed anti-ferromagnetism in AF-LSMO layer.

2. Results and Discussion

5 nm FM-LSMO was deposited underneath 15 nm AF-LSMO, which served as both the bottom electrode and resistance detection layer for EB observations. High-quality thin films with atomically flat surface and interface were demonstrated by high-resolution X-ray diffraction (HRXRD), atomic force microscopy (AFM) image, and high-angle annular dark field (HAADF)-STEM images (Figure S2, Supporting Information).

After confirming the EB in AF-LSMO/FM-LSMO bilayers (Figure S3, Supporting Information), a low-voltage pulsing process was deployed for regulating the sample at 300 K. In each pulse cycle of 800 ms, one gate pulse of width 500 ms is applied. The number of pulses applied in different States, and the magnitude of gate pulse voltage used, are indicated in Figure 2a. All characterizations were conducted after removing the pulses at 300 K in vacuum chamber.

Figure 2b shows the representative MR curves at 20 K of States 1, 2, 6, and 7. Compared with the peak positions of States 1 and 2, the peak positions of MR curve at State 6 are shifted toward zero field, suggesting modulated magnetic properties of AF-LSMO/FM-LSMO. Subsequent applications of -10 V pulses

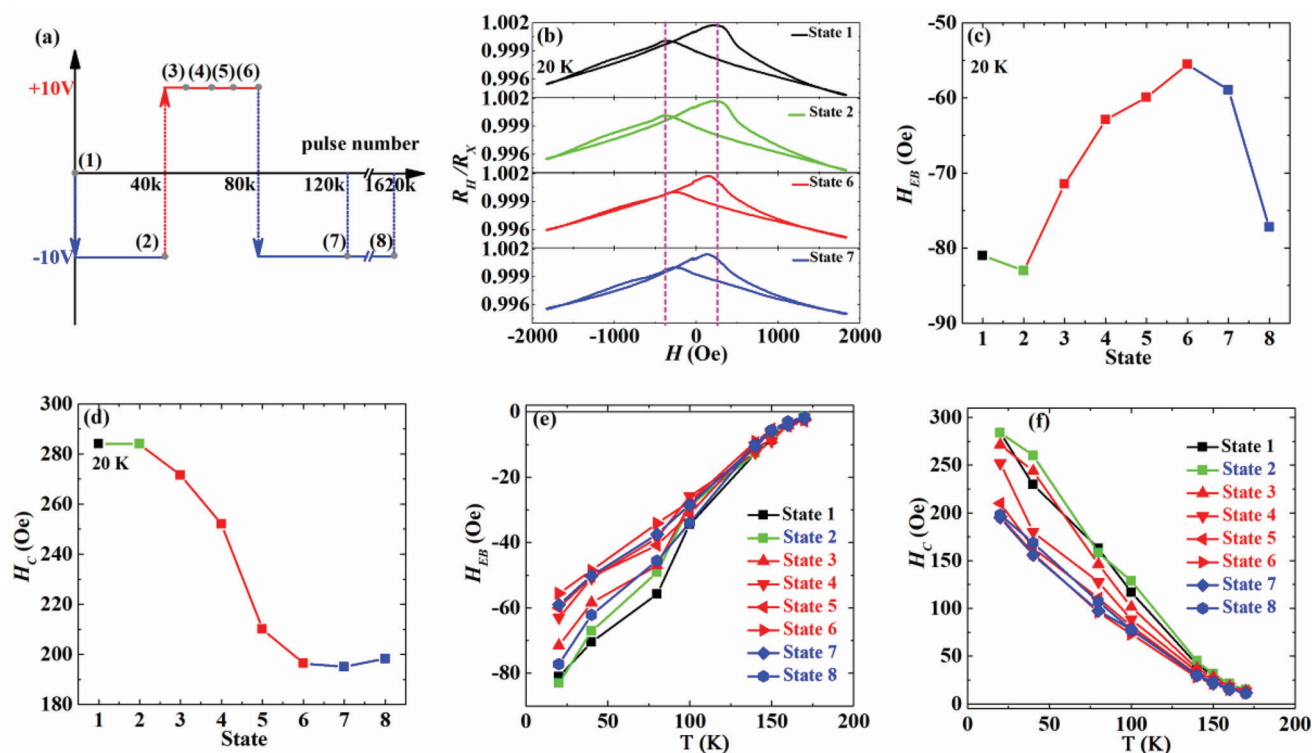


Figure 2. Regulations of EB by low-voltage pulses. a) Illustration of the modulation process. Starting from the pristine state (State 1), 40k pulses of -10 V were applied to the device (State 2). Subsequently, series of 10k pulses of $+10$ V were gradually applied to the sample, resulting in the States 3 to 6. After the positive pulse chains, another 40k of -10 V pulses were applied (State 7). Eventually, 1.5M pulses at -10 V were applied to the device after State 7 and resulting in State 8 of the device. b) Representative MR curves at 20 K for different states. Evolution of H_{EB} and H_C at 20 K in the modulation process is shown at (c) and (d). (e) and (f) are The temperature dependent H_{EB} and H_C for different states, respectively.

(State 7) show a minute change in MR compared with that of State 6.

Figure 2c, shows a detailed comparison of exchange bias field (H_{EB}) and coercivity (H_C) at 20 K for various states. After applying 40k -10 V pulses (from State 1 to 2), both H_{EB} and H_C show no change. Followed by a gradual application of 40k $+10$ V pulses (from State 2 to 6), the absolute value of H_{EB} (H_C) gradually decreases from 83 to 56 Oe (284 to 196 Oe), indicating the suppressed EB in AF-LSMO/FM-LSMO. -10 V pulses are applied (from State 6 to 8) to reverse the EB back to State 1. The absolute value of H_{EB} shows a gradual increase from 56 to 77 Oe, while H_C shows almost no change, suggesting weak reversibility of negative pulses. Compared with other EB systems with electric-field-driven magnetoionic modulation,^[19–22,34–36] the low-voltage pulse regulation by P(VDF-TrFE) dielectric gate presented here is a relatively moderate process. Currently, electric-field-driven magnetoionic modulation of the EB is mainly based on the motion of ions (H^+ and O^{2-}) because of their small ionic radii. Unlike the fast regulation (ms regime) of EB in hydrogen ion migration-based system,^[21] oxygen ion migration-based regulation usually needs a few hours due to larger ionic radius^[34,20] and is consistent with our case. For amorphous bilayer/multilayer systems,^[34,20,19] by applying low voltages across AF oxide layer or electrolyte layer, oxygen ion migration induced modulation of H_{EB} can lead to variations in the order of tens of Oe at room temperature. For epitaxial perovskite bilayer systems,^[35,22] oxygen ion migration is typi-

cally regulated at room temperatures by ionic liquid gating, and the modulation of H_{EB} by a few hundred Oe can be observed at low temperatures, which is much stronger compared with our case. A possible explanation is that a larger charge density ($\approx 10^{15}$ cm^{-2}) can be generated at the interfaces when using IL gating as compared with P(VDF-TrFE) ($\approx 1 \mu\text{C cm}^{-2}$ at 10 V, 6.24×10^{12} cm^{-2}), thus a much stronger electric field is generated across the system.^[37]

Temperature dependent H_{EB} and H_C of bilayers (Figure 2e) show that the magnitude of H_{EB} decreases with increasing temperature until it vanishes at around 170 K (blocking temperature, T_B). The effect of low-voltage pulses on H_{EB} mainly occurs below 100 K. This is related to the magnetic structure of AF-LSMO layer. Previous report on AF-LSMO^[32] suggests an intermediate temperature range (100–250 K) where the complete AF spin structure is not formed due to strain state or chemical disordering. Only below this range, the long-range magnetic ordering of AF-LSMO can be formed. The regulation of temperature dependent H_{EB} again indicates that low-voltage pulses have changed the magnetic properties of AF-LSMO layer. Similarly, regulation of temperature dependent H_C (Figure 2f) also mainly occurs at low temperatures. These electrical transport results demonstrate that positive low-voltage pulses can suppress the EB by regulating the magnetic properties of AF-LSMO layer, while negative ones show weak effect on the EB.

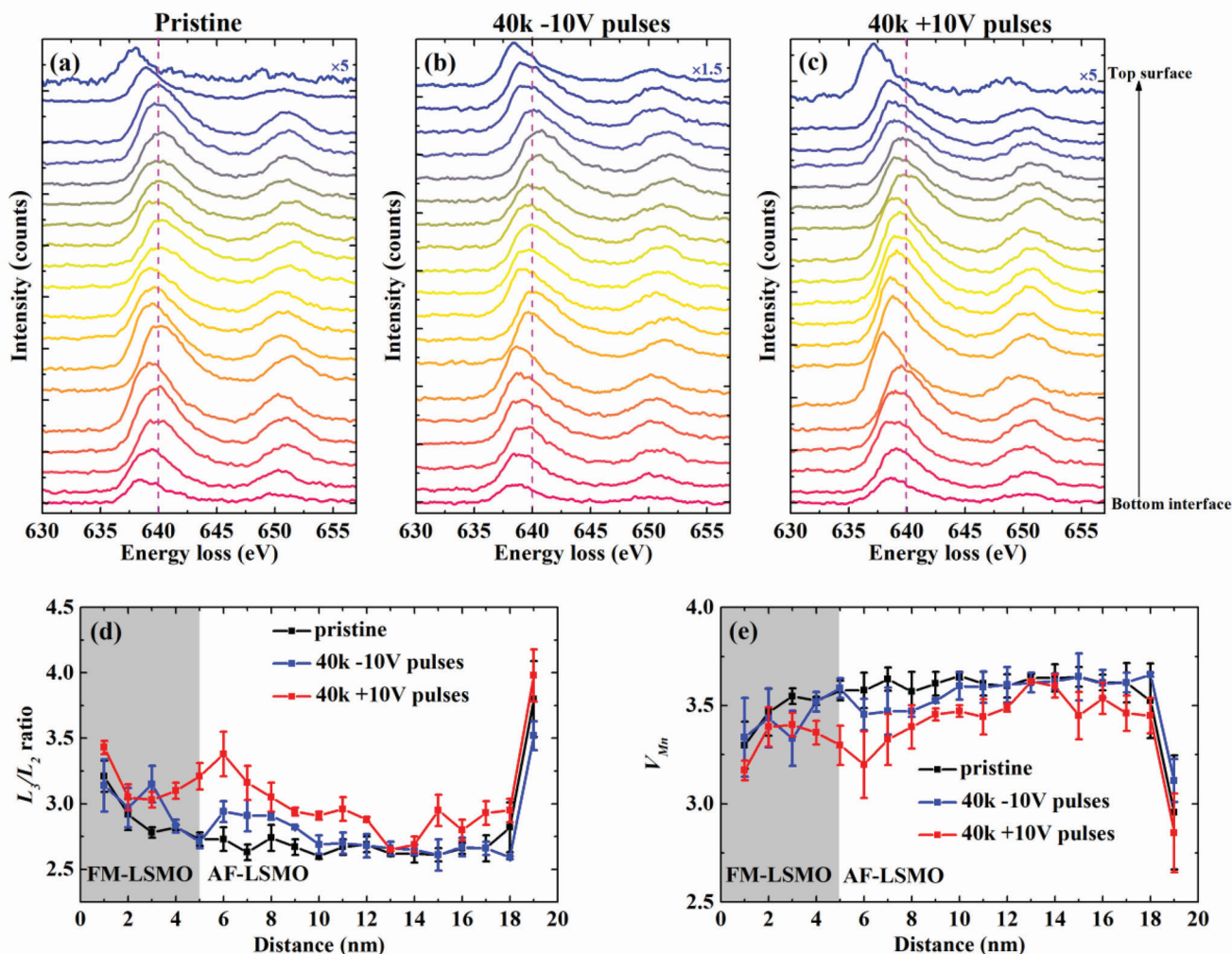


Figure 3. Effect of low-voltage pulses on the electronic change of AF-LSMO/FM-LSMO revealed by STEM-EELS. Mn- $L_{2,3}$ EEL spectra from substrate/FM-LSMO interface to top surface for pristine, 40k –10 V pulsed, and 40k +10 V pulsed samples are shown in (a), (b), and (c), respectively. Extracted L_3/L_2 ratios and corresponding V_{Mn} variation from substrate/FM-LSMO interface to top surface are shown in (d) and (e), respectively.

To ensure the reproducibility of the regulation effect, two additional devices were tested with different gating sequences. Device one (#1) was first applied 40k –10 V pulses and followed by another 40k +10 V pulses. From the transport data in Figure S4, Supporting Information, it can be seen that negative pulses almost have no impact on the EB while positive can strongly suppress H_{EB} (H_C) from –36 Oe (196 Oe) of pristine state to –9 Oe (126 Oe) at 20 K. Meanwhile, T_B is reduced from 150 K of pristine state to 100 K by the application of 40k +10 V pulses.

Device two (#2) was first applied 40k +10 V pulses and then 40k –10 V pulses. From the transport data shown in Figure S5, Supporting Information, after the H_{EB} (H_C) at 20 K being reduced from –114 Oe (332 Oe) of pristine state to –63 Oe (167 Oe) by 40k +10 V pulses, negative pulses cannot revoke the changes.

We note that the EB behavior varies across devices undergoing the same gating processes, which can be seen from the variation of MR curve shape, amplitude of H_{EB} , H_C , and T_B , but would show similar MR ratio (–0.25% at 20 K) within the swept field range, resistivity range (0.002–0.02 Ω cm) from 20 to 300 K, and

T_C around 280 K. Quantitative variation of EB behavior in different devices might result from run-to-run variations, which alters the pinning strength of magnetic moments in FM-LSMO layer. However, transport data in these devices point the same fact that positive pulses can strongly suppress the EB while negative ones can only slightly affect it.

HAADF-STEM and EELS were performed to investigate the effect of low-voltage pulses on the microstructure and oxidation states of Mn ions. Three transmission electron microscopy (TEM) specimens were cut from different regions of the same sample (Figure S6, Supporting Information) to eliminate uncertainties due to sample preparation. To explore the spatial variation of Mn valence state, EELS data were acquired across the film layers. By aligning the pre-peak position of O K edge at 530 eV (Figure S10, Supporting Information), the corresponding Mn L edge white lines were investigated (Figure 3a–c). Note that the first five lines from the bottom interface correspond to FM-LSMO layer, and the rest are attributed to the AF-LSMO layer.

For pristine sample (Figure 3a), the L_3 white lines of AF-LSMO layer shift to higher energy at ≈ 640 eV as compared with FM-LSMO layer, indicating higher oxidation state of Mn and is consistent with the higher Sr doping level in AF-LSMO. The deviation from this trend for the top 2 nm of AF-LSMO can be attributed to intrinsic oxygen vacancies due to surface symmetry breaking.^[38–40] For the 40k –10 V pulsed sample (Figure 3b), similar higher energy shift of Mn L_3 white line from FM-LSMO to AF-LSMO is observed. The L_3 white line does not show obvious shift as compared with the pristine sample. This means –10 V pulses have little effect on the valence state of Mn. In contrast, for 40k +10 V pulsed sample (Figure 3c), almost all the L_3 white lines in AF-LSMO shift to lower energy (≈ 639.1 eV), as compared to the pristine sample. These results suggest that oxygen vacancies are introduced into AF-LSMO layer by 40k +10 V pulses.

Previous studies showed that the L_3/L_2 ratio can be used to extract Mn electronic configuration without considering the absolute energy scale.^[41,42] Thus L_3/L_2 white line ratio (Figure 3d) is extracted to quantitatively identify the influence of low-voltage pulsing on Mn valence (V_{Mn}). To calculate the valence state evolution from bottom interface to top surface (Figure 3e), we use the smallest L_3/L_2 ratio of FM-LSMO layer in the pristine sample as the reference of ideal V_{Mn} in FM-LSMO layer ($V_{Mn} = 3.3$) and the highest L_3/L_2 ratio of pristine sample in AF-LSMO layer as the reference of ideal V_{Mn} in AF-LSMO layer ($V_{Mn} = 3.65$). For the pristine sample, a gradual increase of V_{Mn} in FM-LSMO layer is observed from the bottom, indicating chemical diffusion at FM-LSMO/AF-LSMO interface where reduction of La^{3+}/Sr^{2+} ratio is demonstrated by the interfacial EDX (Figure S8, Supporting Information). For AF-LSMO layer, V_{Mn} is kept constant at around 3.65 throughout the layer, suggesting a uniform charge distribution. Compared with the pristine sample, the negatively-pulsed sample shows a clear increase of V_{Mn} for the top-most layer, suggesting the suppression of oxygen vacancies. Meanwhile, the remaining part of AF-LSMO and the FM-LSMO layer demonstrate almost identical V_{Mn} as compared with that of the pristine sample. However, at some regions in AF-LSMO layer close to the interface (6–9 nm), EELS analysis suggests slight oxygen deficiency. This could explain the slightly-suppressed V_{Mn} in the negatively pulsed sample as measured by X-ray photoelectron spectroscopy (XPS) (Figure S9 and Table S1, Supporting Information). In contrast, positive pulsing results in significant suppression of V_{Mn} compared with pristine sample throughout the AF-LSMO layer, which is also confirmed by the analysis of O K edge fine structure (Figure S11, Supporting Information). From the analysis of EELS data, it is concluded that positive pulses introduce oxygen vacancies throughout AF-LSMO layer. Negative pulses eliminate oxygen vacancies on AF-LSMO surface, but at the same time oxygen vacancies are created near AF-LSMO/FM-LSMO interface.

In general, oxygen vacancies are expected to modulate both V_{Mn} and lattice parameter. While V_{Mn} modulation has been observed in XPS and EELS analyses, strain map (Figure S7, Supporting Information) and XRD (Figure S12, Supporting Information) analysis results have not revealed corresponding changes in lattice parameter. A possible explanation is that the change of lattice parameter is minute and localized that is beyond the detection limit of the strain map and XRD analysis methods.

To further explore on the discrepancy, changes of local lattice environment across the interfaces of AF-LSMO/FM-LSMO/STO

before and after pulsing process was analyzed by multiple-ellipse fitting method.^[43] Here, real-space A-site atoms were chosen for fitting to get the precise atomic position due to its higher intensity in HAADF-STEM images. A HAADF-STEM image around the interfaces of pristine sample is shown in Figure 4a. The corresponding in-plane lattice spacing map (Figure 4b) suggests a uniform in-plane lattice distribution around 3.91 Å, which is consistent with the fully-strained state revealed by strain map in Figure S7, Supporting Information. In contrast, there is stronger localized in-plane lattice variation in AF-LSMO layer around the AF-LSMO/FM-LSMO interface, which could be the result of larger lattice mismatch between AF-LSMO and $SrTiO_3$ (STO) or interfacial element diffusion. The corresponding out-of-plane lattice spacing map (Figure 4c) also reveals a gradual reduction from FM-LSMO to AF-LSMO, which is consistent with the strain map.

The averaged in-plane and out-of-plane lattice constants are plotted in Figure 4d. From FM-LSMO to AF-LSMO, a gradual reduction from 3.91 to 3.82 Å ($\epsilon_{oop} \approx -0.023$) (from 10 to 7 nm in the vertical axis of Figure 4d) is also confirmed just like the strain map result in Figure S7, Supporting Information. Compared with pristine sample, HAADF-STEM image of negative pulse-gated sample (Figure 4e) shows no obvious change. However, the corresponding in-plane lattice spacing map (Figure 4f) displays increased local lattice variation in AF-LSMO layer close to the AF-LSMO/FM-LSMO interface. In the corresponding out-of-plane lattice map (Figure 4g), the increased local lattice variation does not only take place in AF-LSMO but also in FM-LSMO and even STO substrate. The averaged in-plane constant reveals increased in-plane lattice constant from 3.91 to 3.92 Å from 10 to 4 nm in Figure 4h (comparison with pristine sample can be seen in Figure S14, Supporting Information). The averaged out-of-plane constant in Figure 4h reveals increased out-of-plane lattice constant across the whole interface. This means negative pulses not only creates oxygen vacancies in AF-LSMO layer near AF-LSMO/FM-LSMO interface (as revealed by the EELS data in Figure 3), but also regulates the lattice parameter around FM-LSMO/STO interface.

Figure 4i shows the HAADF-STEM image of positive pulses gated sample. The corresponding in-plane and out-of-plane lattice spacing maps in Figure 4j,k also confirm the increased local lattice variation similar to the case of negative pulses gated sample. The averaged in-plane lattice constant shows slight increase from 11 to 7 nm in Figure 4l) (comparison with pristine sample can be seen in Figure S14, Supporting Information). The averaged out-of-plane lattice constant is increased from 11 to 0 nm in Figure 4l. For comparison, Figure 4a,e,i is also analyzed by GPA method (Figure S13, Supporting Information).^[44,45] The local lattice variation between three samples cannot be easily recognized like the real-space fitting method.

In the 40k +10 V pulsed sample, some local areas in AF-LSMO layer close to the AF-LSMO/FM-LSMO interface has implied oxygen deficiency by EELS analysis. Dark stripe-like structures are observed in such regions, and the corresponding HAADF-STEM image of such structure is shown in Figure 5a. In Figure 5a, the dark stripe regions appear along in-plane direction with periodicity of three-unit cells. A reasonable explanation is that oxygen depletion is confined along the out-of-plane direction. Representative regions for stripe-like structure (Figure 5b) were selected for fast-Fourier transformation (FFT) analyses. Figure 5c clearly

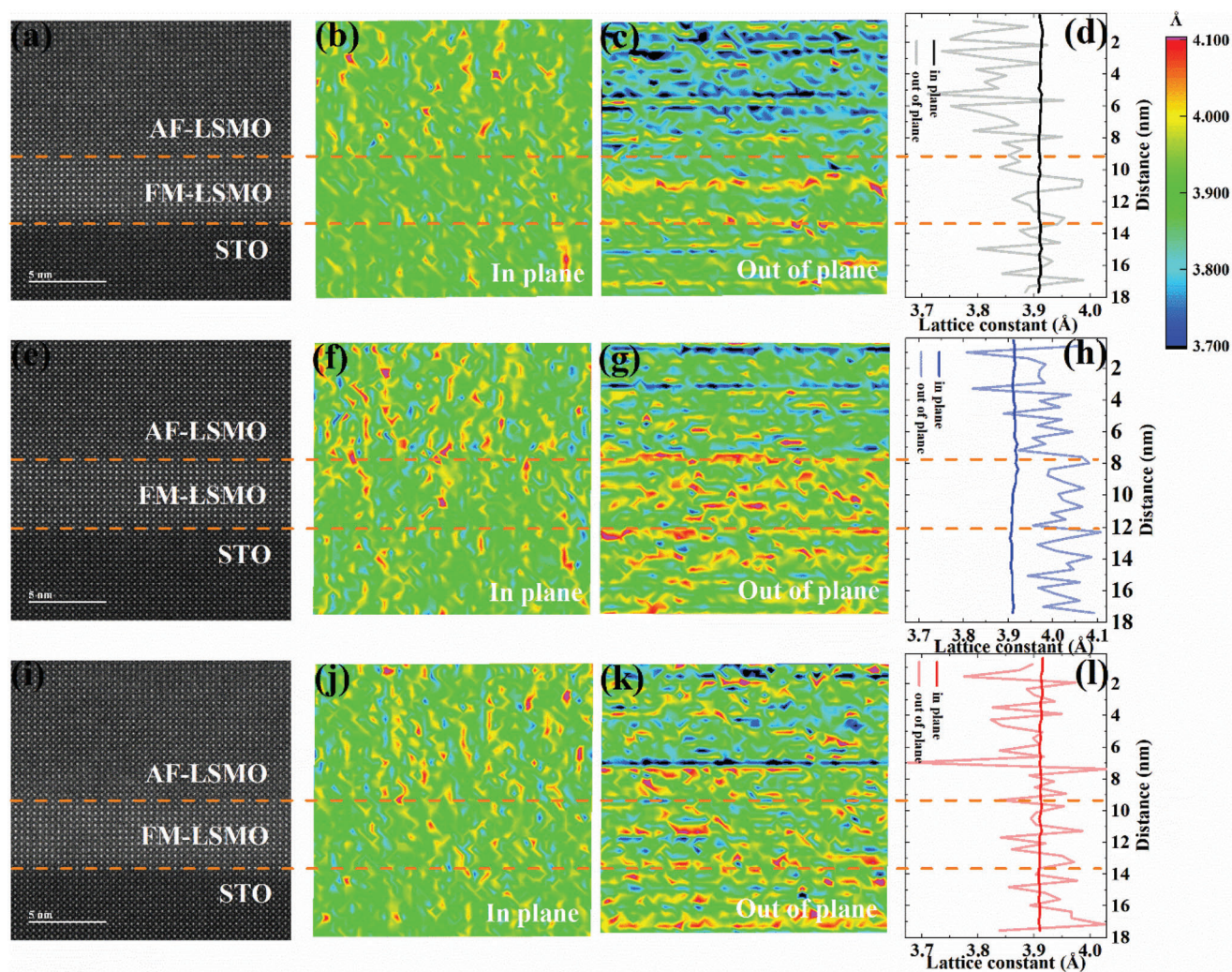


Figure 4. Comparison of local lattice variation before and after pulse gated sample. a) HAADF-STEM image of pristine sample. Corresponding lattice spacing maps of in plane and out of plane are shown in (b) and (c), respectively. d) Averaged in-plane and out-of-plane lattice constant of pristine sample. e) HAADF-STEM image of 40k –10V pulses gated sample. Corresponding lattice spacing maps of in plane and out of plane are shown in (f) and (g), respectively. h) Averaged in-plane and out-of-plane lattice constant of –10V pulsed sample. i) HAADF-STEM image of 40k +10V pulses gated sample. Corresponding lattice spacing maps of in plane and out of plane are shown in (j) and (k), respectively. l) Averaged in-plane and out-of-plane lattice constant of +10V pulsed sample.

reveals an ordered superstructure with a periodicity of three-unit cells, which is quite different from brownmillerite structure with a periodicity of two-unit cells. Space mapping between planes with La/Sr ions for the stripe-like structure is shown in Figure 5d,e. The spacing varies alternatively along in-plane direction (a_1 and a_2 in Figure 5d), while an averaged a value of 3.92 Å equals with c along out-of-plane direction (Figure 5e) is obtained. This can also be found in Figure 4l but with a slightly increased value in Figure 5d,e. These features indicate that a superstructure is formed in AF-LSMO due to confined oxygen vacancies. Similar superstructures with periodicity of three unit cells have been reported in tensile-strained $\text{LaCoO}_{3-\delta}$ thin films with 11% oxygen deficiency ($\delta \approx 0.33$).^[46,47]

Based on the above observations, possible interpretation of low-voltage pulse regulation of EB in AF-LSMO/FM-LSMO is drawn as follows. Both XPS and EELS analyses suggest posi-

tive pulses create oxygen vacancies in AF-LSMO layer. According to previous reports,^[22,23,48–50] two possible mechanisms associated with oxygen vacancies can be responsible for modulating magnetic properties of perovskite manganite: structural defects/disorders and variation of V_{Mn} . Although XRD results on 15 nm AF-LSMO film (Figure S12, Supporting Information) indicate minimal impact of low-voltage pulses, structure defect/disorder are nevertheless observed in the HAADF-STEM images due to the pulsing process, which might contribute to the EB modulation. Such defects include oxygen vacancies (nonmagnetic point defects) and domain boundaries between stripe-like superstructures and normal AF-LSMO structure. According to the domain state theory,^[5,13] increasing nonmagnetic defect concentration favors the formation of magnetic domains and thus leads to increased net magnetization in bulk AF. This results in a rise of H_{EB} until the exchange interaction between the two

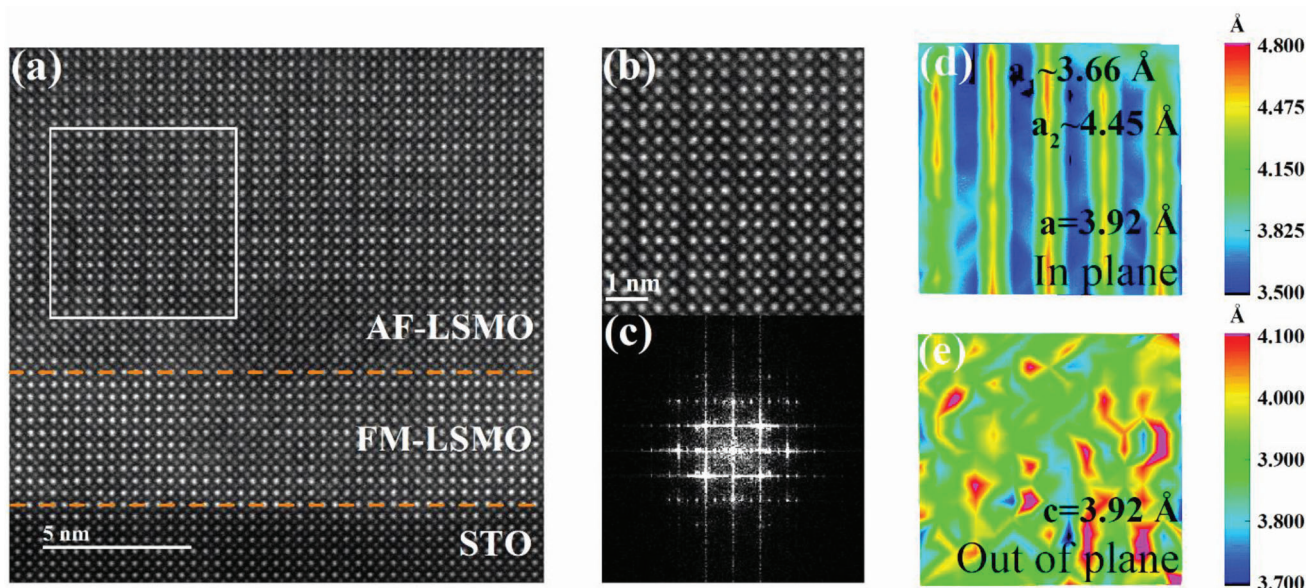


Figure 5. Superstructure in the 40k +10 V pulsed sample. a) Representative HAADF-STEM image of the dark stripe-like structure. b) Enlarged picture of white square circled area. c) Corresponding FFT spots of the area shown in (b). (d) and (e) are the in-plane and out-of-plane lattice spacing maps for the stripe-like structure in (b), respectively.

magnetic sublattices is broken due to excessive nonmagnetic defect concentration. The continuous decrease of H_{EB} upon gradually increasing the number of +10 V pulse (State 2 to State 6) suggests that the structure defect/disorder associated with the oxygen vacancies is not the main reason for EB modulation in our case.

On the other hand, quantitative analyses of XPS and EELS results strongly point out that the variation of V_{Mn} plays a crucial role for modulating EB. In perovskite manganites, magnetism is governed by the exchange interactions between Mn ions through mechanisms such as superexchange (SE) and double exchange (DE).^[51–53] For FM-LSMO, ferromagnetism is dominated by DE between Mn^{3+} and Mn^{4+} ions, while SE between Mn^{4+} ions determines antiferromagnetism in AF-LSMO. This satisfies the prerequisite for the establishment of EB in AF-LSMO/FM-LSMO. Therefore, the variation of V_{Mn} means the change of Mn^{4+}/Mn^{3+} ratio, which in turn determines the strength of either the SE interaction in AF-LSMO or the DE interaction in FM-LSMO.

From the EELS results, it can be seen that positive pulses reduce V_{Mn} in AF-LSMO layer, indicating an increase of Mn^{3+} ions at the expense of Mn^{4+} ions. As a result, the SE-dominated antiferromagnetic coupling is suppressed while the DE-dominated ferromagnetic coupling is enhanced. This is consistent with our experimental observation of suppressed H_{EB} and reduced H_C (alongside with enhanced conductivity around T_C and increased T_C ; Figure S15, Supporting Information) upon positive pulsing. For the negative pulses, the V_{Mn} in AF-LSMO is little affected. This may be related with the difficulty of refilling oxygen ions. Correspondingly, the modulation on EB is very weak because much more pulses are needed to reverse the H_{EB} compared with the effect of positive pulses.

Another issue that should be addressed is whether the variation in FM-LSMO dominates the regulation of EB, since V_{Mn} of top FM-LSMO surface (Figure 3e) and local lattice environ-

ment of FM-LSMO (Figure 4) are also affected by +10V pulses. Assuming the V_{Mn} change and lattice variation of FM-LSMO surface are dominant, a reduced T_C , increased resistivity around T_C , increased MR ratio, and increased EB should be observed. These have not been observed in our results. This again suggests that the reduced V_{Mn} of AF-LSMO should be responsible for the suppression of EB after applying +10 V pulses.

3. Conclusion

In summary, fully strained AF-LSMO/FM-LSMO bilayers with flat interface and surface were prepared. Negative EB was observed at the system. By using electrical transport measurement, in situ regulation of EB was realized via applying low-voltage pulses across a ferroelectric copolymer. XPS, STEM, and EELS techniques revealed that the control of EB in AF-LSMO/FM-LSMO bilayer mainly resulted in modulation of antiferromagnetism in AF-LSMO layer due to creation/annihilation of oxygen vacancy in AF-LSMO layer. This work not only reveals a hidden effect in ferroelectric field effect devices but also shows promises for low electric field regulation of antiferromagnetic spintronics.

4. Experimental Section

Growth of Thin Films: AF-LSMO and FM-LSMO were grown on TiO_2 -terminated STO (001) substrates by pulsed laser deposition with a KrF (wavelength of 248 nm) excimer laser. The growth temperature, oxygen pressure, laser energy, and laser frequency used were 600 °C (for top AF-LSMO)/700 °C (for bottom FM-LSMO), 150 mTorr, 220 mJ, and 1 Hz, respectively. To suppress oxygen vacancies during growth, all samples were post-annealed in 10 Torr oxygen pressure for 5 min after the deposition of all layers.

P(VDF-TrFE) Copolymer Preparation: Transparent P(VDF-TrFE) solution with a mass content of 2.5% was obtained by dissolving P(VDF-TrFE)

powder (70/30, France Piezotech) in diethyl carbonate solvent and stirring for 24 h. 250 nm P(VDF-TrFE) copolymer was obtained by spin-coating the P(VDF-TrFE) solution at 4000 rpm for 30 s. The P(VDF-TrFE) thin film was annealed in oven at 120 °C for 2 h to get the crystalline structure with ferroelectric β phase

Devices Preparation: To prepare the device, photoresist (AZ5214E) was first spin coated on the as grown AF-LSMO/FM-LSMO sample with thickness around 1 μm . Followed by 1 min baking at 110 °C. Then the sample was exposed to UV light for 8 s with SUSS MA6 mask aligner under soft-contact mode. After that, the sample was immersed into AZ MIF 300 developer for 20 s. Thus, the Hall bar pattern with channel size of 50 $\mu\text{m} \times 100 \mu\text{m}$ was transferred on to the surface of AF-LSMO/FM-LSMO. The sample with Hall bar pattern was then immersed in KI/HCl (0.1 mL 0.37 wt% HCl + 5 mL KI 5M in H_2O) etchant for 10 s, followed by DI water leaching to remove the residual etchant. Then the sample was ultrasonically cleaned in acetone, ethanol, and DI water to remove the photoresist. In such a way, AF-LSMO/FM-LSMO was etched into expected Hall bar geometry; followed by a second photolithography to transfer the pattern of contact pads onto the Hall bar. Then Ti(5 nm)/Au(50 nm) was deposited onto the sample surface by electron beam evaporation. By ultrasonic washing in acetone for 1 min, the photoresist as well as Ti/Au layers on the top was removed. Thus, AF-LSMO/FM-LSMO Hall bar with Ti/Au contact pad was prepared. A 250 nm P(VDF-TrFE) dielectric layer was spin-coated on top of Hall bar channel as the gate dielectric. 100 nm Al (top gate electrode) was deposited by electron beam evaporation on top of dielectric layer with shadow mask.

Material Characterizations: X-ray reflectivity (XRR) and HRXRD measurements were conducted by a Rigaku SmartLab (9 kW) machine. The surface morphology was characterized by AFM (Bruker). Specimens for TEM were cut by a focused ion beam microscope from three different locations of the same sample. HAADF-STEM images, EELS, and EDX mappings were acquired using a FEI Titan Themis Z microscope (300 kV) equipped with double correctors. XPS was conducted by a Thermo Fisher Nexsa X-ray Photoelectron Spectrometer with a monochromatic Al source ($K_{\alpha} = 1486.7 \text{ eV}$). Measurements were conducted with the electron flood gun on to eliminate the charging effect. The binding energies were calibrated by the C 1s peak at 248.8 eV.

Data Analysis: XRR data were fitted with GlobalFit (Rigaku) software to get the thickness, density, and surface and interface roughness information. XPS data were analyzed by Avantage (Thermo Fisher Scientific) software. EELS and EDX data were analyzed by DigitalMicrograph software. Details of fitting method of EELS can be found in the previous work.^[54] Strain maps were obtained by FRWR tools software by selecting reflection pair of (110) and (1-10) with resolution and smoothing parameters of 1 and 0.7, respectively. Lattice spacing maps were obtained by multiple-ellipse fitting method with CalAtom software tool after Gaussian filtering background and getting initial atom position with threshold method.^[43]

Magnetoelectrical Transport Measurements: All low-voltage pulses were applied in vacuum at 300 K, and characterizations were conducted after low-voltage pulsing processes. Electrical measurements were conducted on Hall bar devices with a constant current of 1 μA . For MR measurements, $\pm 5000 \text{ Oe}$ in-plane magnetic field parallel to the current direction was applied during the cooling process. Ten training cycles were performed before acquiring the MR data to eliminate the training effect.

Supporting Information

Supporting Information is available from the Wiley Online Library or from the author.

Acknowledgements

This work was supported by the Hong Kong Research Grants Council (PolyU 153027/17P), the Hong Kong Polytechnic University (ZVWC), and Guangdong Special Support Project (2019BT02X030). Y.K.L. acknowledges the Research Fund of Zhaoqing University (No. 2021011832).

L.F. acknowledges support from the National Natural Science Foundation of China (Nos. 51972159 and U21A20500) and the Jiangxi's Natural Science Foundation (Nos. 20212ACB204016, 20192ACB21018, and 20171ACB20006). Z.W. acknowledges the National Natural Science Foundation of China (No. 51702285).

Conflict of Interest

The authors declare no conflict of interest.

Data Availability Statement

The data that support the findings of this study are available from the corresponding author upon reasonable request.

Keywords

exchange bias, low-voltage pulses, oxide antiferromagnetic insulator, oxygen vacancies

Received: April 14, 2023
Revised: May 24, 2023
Published online: July 20, 2023

- [1] W. H. Meiklejohn, C. P. Bean, *Phys. Rev.* **1957**, *105*, 904.
- [2] A. P. Malozemoff, *Phys. Rev. B* **1987**, *35*, 3679.
- [3] D. Mauri, H. C. Siegmann, P. S. Bagus, E. Kay, *J. Appl. Phys.* **1987**, *62*, 3047.
- [4] N. C. Koon, *Phys. Rev. Lett.* **1997**, *78*, 4865.
- [5] P. Miltényi, M. Gierlings, J. Keller, B. Beschoten, G. Güntherodt, *Phys. Rev. Lett.* **2000**, *84*, 4224.
- [6] M. R. Ghadimi, B. Beschoten, G. Güntherodt, *Appl. Phys. Lett.* **2005**, *87*, 261903.
- [7] J. I. Hong, T. Leo, D. J. Smith, A. E. Berkowitz, *Phys. Rev. Lett.* **2006**, *96*, 117204.
- [8] M. Fecioru-Morariu, S. R. Ali, C. Papusoi, M. Sperlich, G. Güntherodt, *Phys. Rev. Lett.* **2007**, *99*, 097206.
- [9] R. Morales, Z.-P. Li, J. Olamit, K. Liu, J. M. Alameda, I. K. Schuller, *Phys. Rev. Lett.* **2009**, *102*, 097201.
- [10] A. C. Basaran, T. Saerbeck, J. de la Venta, H. Huckfeldt, A. Ehresmann, I. K. Schuller, *Appl. Phys. Lett.* **2014**, *105*, 072403.
- [11] M. Y. Khan, C.-B. Wu, W. Kuch, *Phys. Rev. B* **2014**, *89*, 094427.
- [12] T. Shinwari, I. Gelen, Y. A. Shokr, I. Kumberg, M. S. Ikramullah, W. Kuch, M. Y. Khan, *Phys. Status Solidi RRL* **2021**, *15*, 2100195.
- [13] U. Nowak, K. D. Usadel, J. Keller, P. Miltényi, B. Beschoten, G. Güntherodt, *Phys. Rev. B* **2002**, *66*, 014430.
- [14] P. Borisov, A. Hochstrat, X. Chen, W. Kleemann, C. Binek, *Phys. Rev. Lett.* **2005**, *94*, 117203.
- [15] X. He, Y. Wang, N. Wu, A. N. Caruso, E. Vescovo, K. D. Belashchenko, P. A. Dowben, C. Binek, *Nat. Mater.* **2010**, *9*, 579.
- [16] V. Laukhin, V. Skumryev, X. Martí, D. Hrabovsky, F. Sánchez, M. V. García-Cuenca, C. Ferrater, M. Varela, U. Lüders, J. F. Bobo, J. Fontcuberta, *Phys. Rev. Lett.* **2006**, *97*, 227201.
- [17] S. M. Wu, S. A. Cybart, P. Yu, M. D. Rossell, J. X. Zhang, R. Ramesh, R. C. Dynes, *Nat. Mater.* **2010**, *9*, 756.
- [18] S. M. Wu, S. A. Cybart, D. Yi, J. M. Parker, R. Ramesh, R. C. Dynes, *Phys. Rev. Lett.* **2013**, *110*, 067202.
- [19] L. Wei, Z. Hu, G. Du, Y. Yuan, J. Wang, H. Tu, B. You, S. Zhou, J. Qu, H. Liu, R. Zheng, Y. Hu, J. Du, *Adv. Mater.* **2018**, *30*, 1801885.

- [20] J. Zehner, R. Huhnstock, S. Oswald, U. Wolff, I. Soldatov, A. Ehresmann, K. Nielsch, D. Holzinger, K. Leistner, *Adv. Electron. Mater.* **2019**, 5, 1900296.
- [21] J. Zehner, D. Wolf, M. U. Hasan, M. Huang, D. Bono, K. Nielsch, K. Leistner, G. S. D. Beach, *Phys. Rev. Mater.* **2021**, 5, L061401.
- [22] B. Cui, C. Song, F. Li, X. Y. Zhong, Z. C. Wang, P. Werner, Y. D. Gu, H. Q. Wu, M. S. Saleem, S. S. P. Parkin, F. Pan, *Phys. Rev. Appl.* **2017**, 8, 044007.
- [23] H. Ji, G. Zhou, X. Wang, J. Zhang, P. Kang, X. Xu, *ACS Appl. Mater. Interfaces* **2021**, 13, 15774.
- [24] R. C. G. Naber, C. Tanase, P. W. M. Blom, G. H. Gelinck, A. W. Marsman, F. J. Touwslager, S. Setayesh, D. M. de Leeuw, *Nat. Mater.* **2005**, 4, 243.
- [25] A. Mardana, S. Ducharme, S. Adenwalla, *Nano Lett.* **2011**, 11, 3862.
- [26] I. Stolichnov, S. W. E. Riestler, E. Mikheev, N. Setter, A. W. Rushforth, K. W. Edmonds, R. P. Campion, C. T. Foxon, B. L. Gallagher, T. Jungwirth, H. J. Trodahl, *Phys. Rev. B* **2011**, 83, 115203.
- [27] P. Nukala, M. Ahmadi, Y. Wei, S. de Graaf, E. Stylianidis, T. Chakraborty, S. Matzen, H. W. Zandbergen, A. Björling, D. Mannix, D. Carbone, B. Kooi, B. Noheda, *Science* **2021**, 372, 630.
- [28] H. Ni, M. Zheng, L. Chen, W. Huang, Y. Qi, J. Zeng, Z. Tang, H. Lu, J. Gao, *Appl. Phys. Lett.* **2017**, 110, 213503.
- [29] Y.-C. Li, D.-F. Pan, J. Wu, Y.-B. Li, G.-H. Wang, J.-M. Liu, J.-G. Wan, *Appl. Phys. Lett.* **2016**, 109, 172904.
- [30] H. F. Wong, S. M. Ng, W. F. Cheng, Y. Liu, X. Chen, D. von Nordheim, C. L. Mak, J. Dai, B. Ploss, C. W. Leung, *Solid State Electron.* **2017**, 138, 56.
- [31] H. F. Wong, S. M. Ng, W. Zhang, Y. K. Liu, P. K. J. Wong, C. S. Tang, K. K. Lam, X. W. Zhao, Z. G. Meng, L. F. Fei, W. F. Cheng, D. von Nordheim, W. Y. Wong, Z. R. Wang, B. Ploss, J.-Y. Dai, C. L. Mak, A. T. S. Wee, C. W. Leung, *ACS Appl. Mater. Interfaces* **2020**, 12, 56541.
- [32] X. W. Zhao, H. F. Wong, Y. K. Liu, S. M. Ng, J. M. Liang, K. K. Lam, W. F. Cheng, C. L. Mak, C. W. Leung, *IEEE Trans. Magn.* **2022**, 58, 4200205.
- [33] H. Y. Hwang, S.-W. Cheong, P. G. Radaelli, M. Marezio, B. Batlogg, *Phys. Rev. Lett.* **1995**, 75, 914.
- [34] P. D. Murray, C. J. Jensen, A. Quintana, J. Zhang, X. Zhang, A. J. Grutter, B. J. Kirby, K. Liu, *ACS Appl. Mater. Interfaces* **2021**, 13, 38916.
- [35] M. S. Saleem, B. Cui, C. Song, Y. M. Sun, Y. D. Gu, R. Q. Zhang, M. U. Fayaz, X. F. Zhou, P. Werner, S. S. P. Parkin, F. Pan, *ACS Appl. Mater. Interfaces* **2019**, 11, 6581.
- [36] X. Zhou, Y. Yan, M. Jiang, B. Cui, F. Pan, C. Song, *J. Phys. Chem. C* **2016**, 120, 1633.
- [37] C. Leighton, *Nat. Mater.* **2019**, 18, 13.
- [38] A. Sadoc, B. Mercey, C. Simon, D. Grebille, W. Prellier, M.-B. Lepetit, *Phys. Rev. Lett.* **2010**, 104, 046804.
- [39] M. J. Calderon, L. Brey, F. Guinea, *Phys. Rev. B* **1999**, 60, 6698.
- [40] J. J. Peng, C. Song, F. Li, Y. D. Gu, G. Y. Wang, F. Pan, *Phys. Rev. B* **2016**, 94, 214404.
- [41] M. Varela, M. P. Oxley, W. Luo, J. Tao, M. Watanabe, A. R. Lupini, S. T. Pantelides, S. J. Pennycook, *Phys. Rev. B* **2009**, 79, 085117.
- [42] Z. Li, M. Bosman, Z. Yang, P. Ren, L. Wang, L. Cao, X. Yu, C. Ke, M. B. H. Breese, A. Rusydi, W. Zhu, Z. Dong, Y. L. Foo, *Adv. Funct. Mater.* **2012**, 22, 4312.
- [43] Q. Zhang, L. Y. Zhang, C. H. Jin, Y. M. Wang, F. Lin, *Ultramicroscopy* **2019**, 202, 114.
- [44] M. J. Hytch, E. Snoeck, R. Kilaas, *Ultramicroscopy* **1998**, 74, 131.
- [45] F. Hue, M. Hytch, H. Bender, F. Houdellier, A. Claverie, *Phys. Rev. Lett.* **2008**, 100, 156602.
- [46] N. Biškup, J. Salafranca, V. Mehta, M. P. Oxley, Y. Suzuki, S. J. Pennycook, S. T. Pantelides, M. Varela, *Phys. Rev. Lett.* **2014**, 112, 087202.
- [47] M. Meng, Y. Sun, Y. Li, Q. An, Z. Wang, Z. Lin, F. Yang, X. Zhu, P. Gao, J. Guo, *Nat. Commun.* **2021**, 12, 2447.
- [48] B. Cui, C. Song, G. Wang, Y. Yan, J. Peng, J. Miao, H. Mao, F. Li, C. Chen, F. Zeng, F. Pan, *Adv. Funct. Mater.* **2014**, 24, 7233.
- [49] S. Chen, H. Zhou, X. Ye, Z. Chen, J. Zhao, S. Das, C. Klewe, L. Zhang, E. Lupi, P. Shafer, E. Arenholz, D. Jin, H. Huang, Y. Lu, X. Li, M. Wu, S. Ke, H. Xu, X. Zeng, C. Huang, L. W. Martin, L. Chen, *Adv. Funct. Mater.* **2019**, 29, 1907072.
- [50] L. Cao, O. Petravic, P. Zakalek, A. Weber, U. Rücker, J. Schubert, A. Koutsoubas, S. Mattauch, T. Brückel, *Adv. Mater.* **2019**, 31, 1806183.
- [51] P. W. Anderson, *Phys. Rev.* **1950**, 79, 350.
- [52] J. B. Goodenough, *Phys. Rev.* **1955**, 100, 564.
- [53] C. Zener, *Phys. Rev.* **1951**, 81, 440.
- [54] X. W. Zhao, S. M. Ng, L. W. Wong, H. F. Wong, Y. K. Liu, W. F. Cheng, C. L. Mak, J. Zhao, C. W. Leung, *Appl. Phys. Lett.* **2022**, 121, 162406.